

Review

Silicon-Nanowire-Based 100-GHz-Spaced 16 λ DWDM, 800-GHz-Spaced 8 λ LR-8, and 20-nm-Spaced 4 λ CWDM Optical Demultiplexers for High-Density Interconnects in Datacenters

Seok-Hwan Jeong

Department of Semiconductor Engineering, The University of Suwon, Hwaseong 18323, Republic of Korea; jeong@suwon.ac.kr

Abstract: Several types of silicon-nanowire-based optical demultiplexers (DeMUXs) for use in short-reach targeted datacenter applications were proposed and their spectral responses were experimentally verified. First, a novel 100-GHz-spaced 16 λ polarization-diversified optical DeMUX consisting of 2 λ delayed interferometer (DI) type interleaver and 8 λ arrayed waveguide gratings will be discussed in the spectral regimes of C-band, together with experimental characterizations showing static and dynamic spectral properties. Second, a novel 800-GHz-spaced 8 λ optical DeMUX was targeted for use in LR (long reach) 400 Gbps Ethernet applications. Based on multiple cascade-connected DIs, by integrating the extra band elimination cutting area, discontinuous filtering response was analytically identified with a flat-topped spectral window and a low spectral noise of < -20 dB within an entire LR-8 operating wavelength range. Finally, a 20-nm-spaced 4 λ coarse wavelength division multiplexing (CWDM)-targeted optical DeMUX based on polarization diversity was experimentally verified. The measurement results showed a low excessive loss of 1.0 dB and a polarization-dependent loss of 1.0 dB, prominently reducing spectral noises from neighboring channels by less than -15 dB. Moreover, TM-mode elimination filters were theoretically analyzed and experimentally confirmed to minimize unwanted TM-mode-oriented polarization noises that were generated from the polarization-handling device. The TM-mode elimination filters functioned to reduce polarization noises to much lower than -20 dB across the entire CWDM operating window.



Citation: Jeong, S.-H.

Silicon-Nanowire-Based
100-GHz-Spaced 16 λ DWDM,
800-GHz-Spaced 8 λ LR-8, and
20-nm-Spaced 4 λ CWDM Optical
Demultiplexers for High-Density
Interconnects in Datacenters.
Photonics **2024**, *11*, 336. <https://doi.org/10.3390/photonics11040336>

Received: 7 March 2024

Revised: 31 March 2024

Accepted: 3 April 2024

Published: 5 April 2024



Copyright: © 2024 by the author. Licensee MDPI, Basel, Switzerland. This article is an open access article distributed under the terms and conditions of the Creative Commons Attribution (CC BY) license (<https://creativecommons.org/licenses/by/4.0/>).

Keywords: silicon photonics; optical waveguide; optical filter; demultiplexer; optical interconnection

1. Introduction

In light of recent increases in data traffic spurred by digital transformation and the advent of 6G mobile communication networks, there is a growing demand for more advanced optical multiplexing technologies like wavelength division multiplexing (WDM) or coherent phase modulation techniques, particularly in datacenter applications [1–9]. Silicon photonics stands out as a highly promising technological platform for the development of photonic integrated circuits (PICs) characterized by high bandwidth and low energy consumption. Considering silicon-based PICs [8–15], together with several photonic components such as laser diodes, optical modulators, and photodetectors, optical waveguide type demultiplexers (DeMUXs) such as microring resonators [16–19], delayed interferometers (DIs) [20–36], or arrayed waveguide gratings (AWGs) [37–48] are normally needed to filter the WDM optical signals spatially out to each photodetector to be decoded.

Various WDM specifications, such as dense WDM (DWDM) and coarse WDM (CWDM), have emerged based on factors like channel count, channel spacing, and channel grid. Given that the DeMUX must cling to these specific requisites to function effectively as a spatial wavelength filter, its configuration needs optimization for each WDM specification. Additionally, concerning optical receivers, the polarization state of signals passing through standard single-mode fibers (SMFs) is not preserved upon coupling to each receiver end. Consequently, an optical DeMUX located on the receiver end becomes essential for handling

arbitrarily polarized optical signals [18,30,38,40,42,49–52]. Several approaches have been devised to address WDM signals at the receiver end, including depolarized [28,30,40] or polarization diversity schemes [35,36,47,49].

This paper provides an overview of three silicon-nanowire-type DI-based optical DeMUXs tailored for datacenter applications: (1) a 100-GHz-spaced 16λ DWDM optical DeMUX [49], (2) an 800-GHz-spaced 8λ long reach 8 (LR-8) optical DeMUX [34], and (3) a 20-nm-spaced 4λ CWDM optical DeMUX [35,36]. We explore their functional advantages and identify technical aspects warranting further investigation compared to previous works. Section 2 is devoted to describing the silicon-nanowire-based polarization splitter-rotator (PSR) responsible for handling arbitrary polarization input signals. Section 3 presents the device scheme, operational principles, and experimental characterizations of the 100-GHz-spaced 16λ DWDM optical DeMUX. Section 4 focuses on theoretical discussions regarding the 800-GHz-spaced 8λ LR-8 optical DeMUX. Section 5 addresses the 20-nm-spaced 4λ CWDM optical DeMUX, particularly examining insertion loss (IL) and polarization crosstalk.

2. Silicon-Nanowire-Based PSR for Polarization Diversity

Typically, a silicon-nanowire waveguide exhibits a compressed core shape, resulting in significant structural birefringence [35,53,54]. This relatively high birefringence enhances the efficiency of polarization diversity [35,36,49] compared to alternative methods such as birefringence elimination [28] or birefringence compensation [30,40]. Illustrated in Figure 1 is a schematic depiction of the silicon-nanowire-based polarization splitter-rotator (PSR) for polarization diversity operation at the receiver end. The PSR comprises a hybrid mode conversion region utilizing rib-shaped silicon-nanowire waveguides [35,51,52] and a mode split region employing a rectangle-shaped silicon-nanowire asymmetric directional coupler (ADC). It is established that the ADC enables randomly linear-polarization (i.e., the linear mixing of TE_{00} and TM_{00} modes) to separate into two outputs with TE_{00} fundamental modes [51,52]. In Ref. [51], normally, shallow-etched rib and normal channel waveguides are utilized for the PSR based on hybrid mode conversion. Such a waveguide shape can be readily fabricated using the currently available complementary metal–oxide–semiconductor (CMOS) foundry process [55].

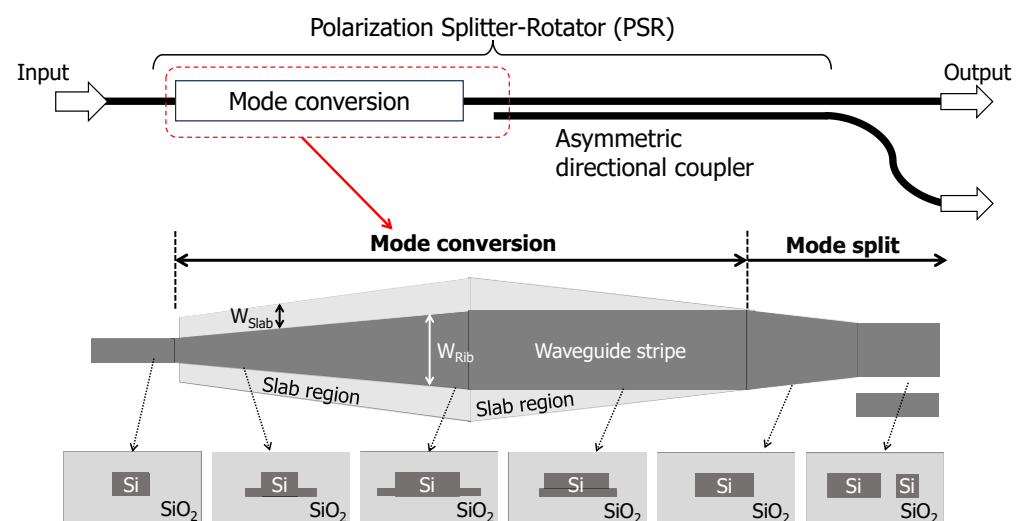


Figure 1. Schematic of silicon-nanowire-based PSR based on mode conversion and mode split.

Figure 2 depicts the simulated propagation mode characteristics: (a) the cross-section view of the low etched silicon-nanowire waveguide and (b) the simulated equivalent refractive indices (N_{eq}) for typical propagation modes in the silicon-nanowire waveguide shown in (a) against the width of waveguide stripe (W_{rib}). Packaged software based on a finite element method (FemSIMTM; Synopsys, CA, USA) was used for implementing the

numerical simulation shown in Figure 2b. For the simulation model illustrated in Figure 2a, the silicon core thickness (T_{Si}), thin layer thickness (T_{Slab}), and thin layer width (W_{Slab}) were set to 220, 90, and 100 nm, respectively. As indicated in Figure 2b, the mode profile continues to preserve as TE_{00} mode irrespective of the value of W_{rib} , while the TM_{00} mode undergoes hybrid mode states, exhibiting both polarizations from TM_{00} mode to TE_{01} higher mode at a certain W_{rib} of approximately $0.55 \mu\text{m}$. That is, only the TM_{00} -mode state is coupled to the TE_{01} mode by adiabatically changing the values of W_{rib} and W_{Slab} . We leverage this TM_{00} -to- TE_{01} -mode conversion to segregate the two input polarization modes into spatially distinct output channels. The number of modes displayed in Figure 2b were restricted to three typical states. It should be noted that the contribution of other higher order modes can be neglected since the main two states of polarization are difficult to couple to any other higher order polarization states.

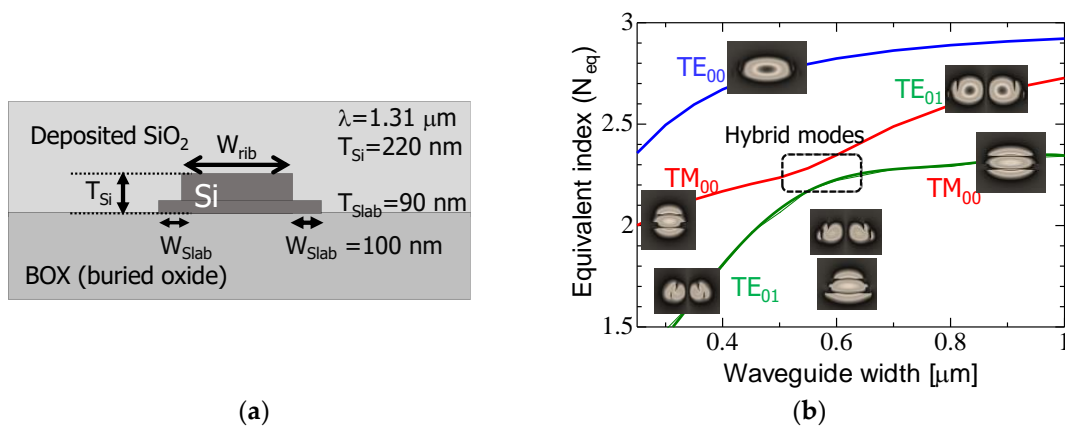


Figure 2. Typical propagation mode properties: (a) cross-section of rib-shaped silicon-nanowire waveguide and (b) calculated equivalent refractive indices (N_{eq}) for existing propagation mode for a waveguide shown in (a) against a width of the waveguide stripe.

Meanwhile, as schematically shown in Figures 1 and 2, the hybrid mode conversion within the PSR needs the shallow-etched rib waveguide structure whose slab width is properly defined. Compared with the channel waveguide scheme formed using a one-time lithography process, the shallow-etched rib waveguides require double-step lithography patterning, which can make the fabrication process somewhat complicated. However, as described in Ref. [55], such double patterning structures are stably controlled by the commercially available silicon photonics foundry process based on ArF-dry lithography process technology. Moreover, considering more advanced ArF-immersion lithography technologies as explained in Ref. [54], the double patterning structures would be no obstacle for densely integrated high-performance circuits.

In this investigation, we devised, theoretically identified, and experimentally validated two varieties of ADC structures [36]. Figure 3 shows the simulated propagation characteristics for the above-mentioned ADC-based mode split areas: (a) the long-length ADC (L-ADC)-based mode split area and the structure parameters for the taper-type L-ADC, (b) the propagating mode profile along the full L-ADC region ($\lambda_{in} = 1.31 \mu\text{m}$), (c) the short-length ADC (S-ADC)-based mode split area, and (d) the propagating mode profile along the full S-ADC region ($\lambda_{in} = 1.31 \mu\text{m}$). A packaged software based on a three-dimensional beam propagation method (3D-BPM, BeamPROPTM; Synopsys, CA, USA) was utilized for the numerical analyses shown in Figure 3b,d. For the L-ADC scenario, the W_{Gap} value was selected to make fabrication easier in the currently used foundry process, whereas the W_A , W_{B1} , and W_{B2} values were adjusted to enable TE_{01} -mode transferring to neighboring waveguides. Conversely, for the S-ADC scenario, the W_C and W_D values were fine-tuned to ensure efficient perfect mode coupling for the specified W_{Gap} condition.

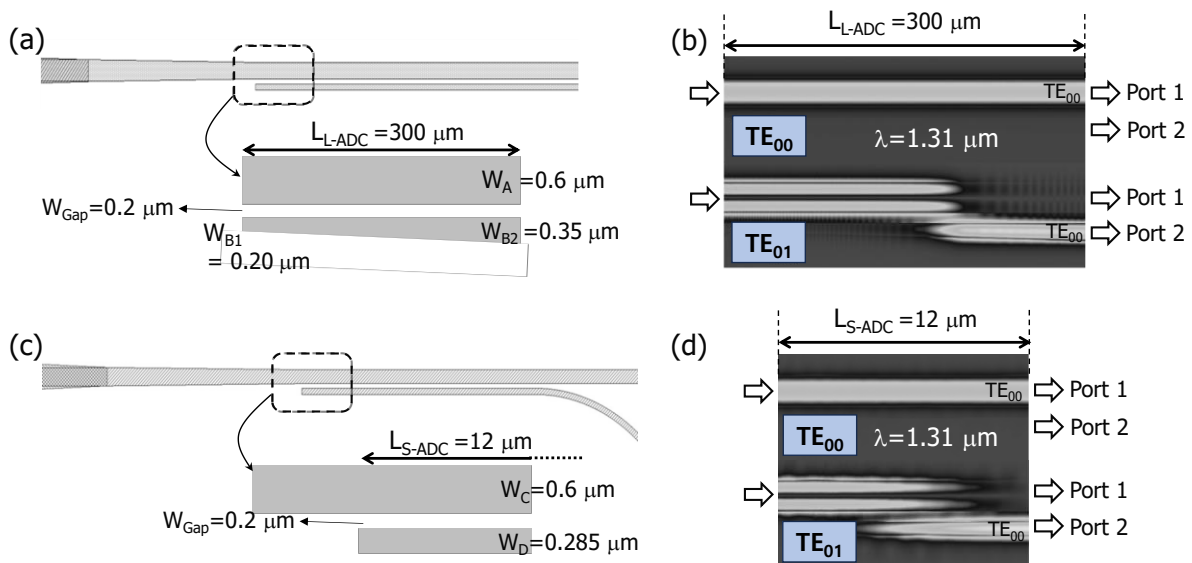


Figure 3. Mode split areas in the PSR and mode propagation at each mode split area: (a) mode split area based on long-length asymmetric directional coupler (L-ADC), (b) simulated mode profile along the L-ADC region ($\lambda = 1.31 \mu\text{m}$), (c) mode split area based on short-length ADC (S-ADC), and (d) simulated mode profiles along the S-ADC region ($\lambda = 1.31 \mu\text{m}$).

Achieving TE_{00} -mode coupling to an adjacent nanowire poses challenges because of the notable index mismatching between the two coupled nanowires in the ADC configuration. However, in two scenarios depicted in Figure 3 (L-ADC and S-ADC), the optimization of the narrower waveguide width makes index matching easier between the TE_{00} -mode and TE_{01} -mode. This enables the TE_{01} -mode, converted from the TM_{00} -mode, to be interacted to the counterpart output channel as TE_{00} -mode. Consequently, arbitrarily polarized input signals can be transferred as TE_{00} -mode output port in the PSR (Figure 3b,d).

The L-ADC depicted in Figure 3b employs a linear tapering technique within a narrower nanowire side, which enables different wavelength components to achieve similar index matching by gradually widening the waveguide from W_{B1} to W_{B2} along the $L_{\text{L-ADC}}$, spanning $300 \mu\text{m}$. As a result, the operational wavelength range of the PSR could be expanded. Put simply, the L-ADC scheme demonstrates greater resilience to variations in coupled waveguide parameters stemming from fabrication imperfections. As illustrated in Figure 3b, when utilizing the parameters outlined in Figure 3a, only TE_{01} -mode transfers to couple to the neighboring nanowire, while TE_{00} -mode traverses the ADC region without undergoing any interaction on mode coupling.

The S-ADC depicted in Figure 3c adopts a structure without any tapering. By optimizing parameters such as the W_C , W_D , and W_{Gap} of the coupled waveguides for a particular wavelength ($\lambda = 1.31 \mu\text{m}$), the coupling length ($L_{\text{S-ADC}}$) can be decreased to $12 \mu\text{m}$, which is shorter than that of the L-ADC by a factor of 25. One possible shortcoming of the S-ADC scheme, however, is its slightly lower allowance for fabrication errors. In this study, the ADC design was carefully selected based on the fabrication precision required for both the PSR and the optical DeMUXs (i.e., S-ADC in the PSR for the 100-GHz-spaced 16λ DWDM optical DeMUX, and L-ADC in the PSR for the 20-nm-spaced 4λ CWDM optical DeMUX).

Currently, mode split areas based on the L-ADC and the S-ADC have a trade-off relation between a small footprint and operating wavelength range. Meanwhile, recently, by adopting a metamaterial scheme engineered by means of structural anisotropy or a slot waveguide structure, an extremely small footprint and wide operating wavelength window for silicon-nanowire-based polarization-handling components, such as polarization beam splitters, have been actively reported [56–59]. Incorporating such anisotropic configuration into the mode conversion and mode split areas could further enhance the performance

of the PSR from the viewpoint of device footprint, operating wavelength range, and fabrication tolerance.

3. 100-GHz-Spaced 16λ DWDM Optical DeMUX

Previous studies have noted that DI-based optical DeMUXs offer technical benefits, including a compact footprint, minimal IL, low spectral crosstalk, and a flat-topped spectral response [20–36]. However, these advantages tend to diminish when the channel count exceeds 8 and the channel spacing narrows below 400 GHz, especially when the optical demultiplexing function is achieved passively rather than through external active control [15].

In our earlier studies, several types of silicon-nanowire-based optical DeMUXs utilizing cascade-connected multiple DIs [22–24] and arrayed waveguide gratings (AWGs) [41,42] were reported. To enhance the WDM transmission capability further, increasing the channel count (N_{Ch}) of DeMUX is necessary. Typically, augmenting N_{Ch} in AWGs is straightforward. However, as N_{Ch} increases, IL and filter spectral uniformity tend to degrade [43,44]. While enhancing the free-spectral range (FSR) of the AWG could be one of solutions to improve IL and spectral uniformity, it might significantly enlarge the footprint to maintain filter specifications such as bandwidth and spectral noises [43].

Introducing another way to address the aforementioned issue, we devised a novel DeMUX configuration comprising box-like spectral DI-type optical interleavers and pairs of AWGs. Through the incorporation of an 8λ-AWG and a flat-topped interleaver, we effectively discriminate between two 8λ spectral bands separated by the FSR of the AWG. This allows us to double the channel expandability of the optical DeMUX to 16λ without compromising on IL and channel uniformity. The schematic of the polarization-diversified 16λ optical DeMUX [49] is shown in Figure 4. For polarization diversity, the PSR discussed in Section 2 was integrated into the optical DeMUXs. The configuration includes the identical DI-type flat-topped optical interleavers and the identical counter-propagating-type 8λ-AWGs, which gives a total output channel number of 32, as indicated in Figure 4.

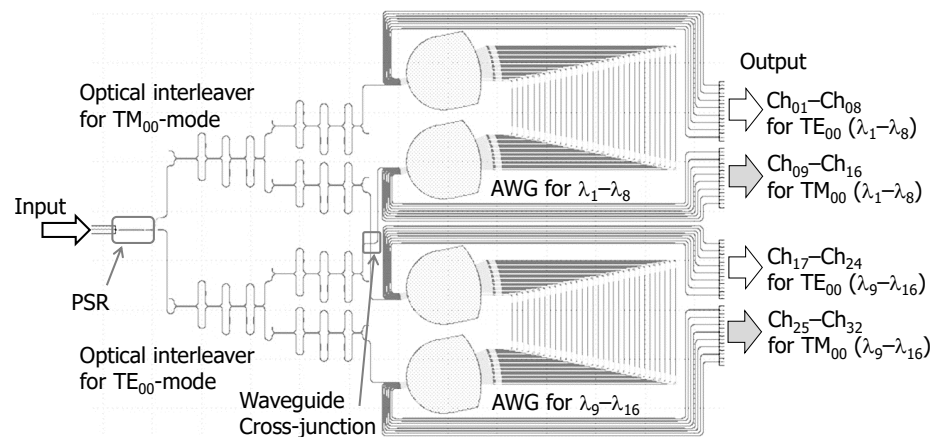


Figure 4. Schematic of polarization diversified silicon-nanowire-based 16λ optical DeMUX consisting of a PSR, two DI-type flat-topped interleavers, and counter-propagating type 8λ-AWGs.

Randomly polarized signals are processed into the spatially separated ports with TE_{00} -mode. Subsequently, each TE_{00} -mode light undergoes processing using identical wavelength filters. In order to ensure the precise alignment of the filtering peaks between the two different polarization inputs, we devised both optical signals to be handled by the counter-propagating type 8λ-AWG whose light paths are the same, which guarantees minimal polarization-sensitive wavelength shift [42]. Notably, the device inherently incorporates a cross-junction to enable a compact polarization-diversified configuration. The crossover shape was designed to minimize the size of crossover, excessive loss (<0.1 dB), and leakage at the crossover (<−30 dB) [23].

Since the 16λ optical DeMUX requires phase accuracy caused by relatively long interaction lengths, as seen in Figure 5, ArF-immersion lithography technology featuring CMOS 40 nm node was adopted to fabricate the devices on a 300 mm SOI (silicon-on-insulator) waferscale with a 200-nm-thick silicon core layer and a 2- μm -thick BOX (buried oxide) layer [53,54]. Figure 5 illustrates the fabricated polarization-diversified silicon-nanowire-based 16λ optical DeMUX, maintaining the entire structure shown in Figure 4. The footprint was calibrated at 1.68 mm in width and 2.85 mm in length, encompassing the PSR, the two DI-type optical interleavers, and the 8λ -AWGs with a waveguide crossover. The S-ADC scheme was employed in the PSR for mode splitting, as the highly accurate ArF-immersion lithography process compensates for a relatively smaller fabrication tolerance for the S-ADC structure. Also, dummy tiles were used for fabrication accuracy.

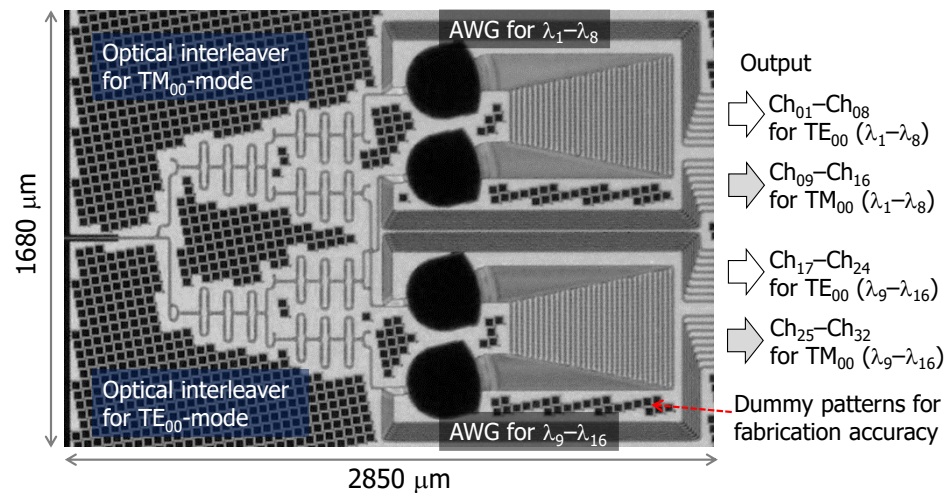


Figure 5. Fabricated 16λ optical DeMUX schematically shown in Figure 4.

Figure 6 displays the spectral characteristics obtained from measurements, with solid and broken lines representing the transmittances for TE_{00} and TM_{00} mode input, respectively. It is worth noting that the transmittance depicted in Figure 6 indicates the transmittivity subtracted by that of a bending-shaped single-mode waveguide for both polarization inputs. In other words, the transmittivity in Figure 6 accounts for the excessive loss resulting from various filter architectures such as the PSR, the DI-based interleavers, and the AWGs. Given that the propagation loss of the waveguide is <0.5 dB/cm through the fabrication process [54], the IL can be regarded as the excessive loss of the device.

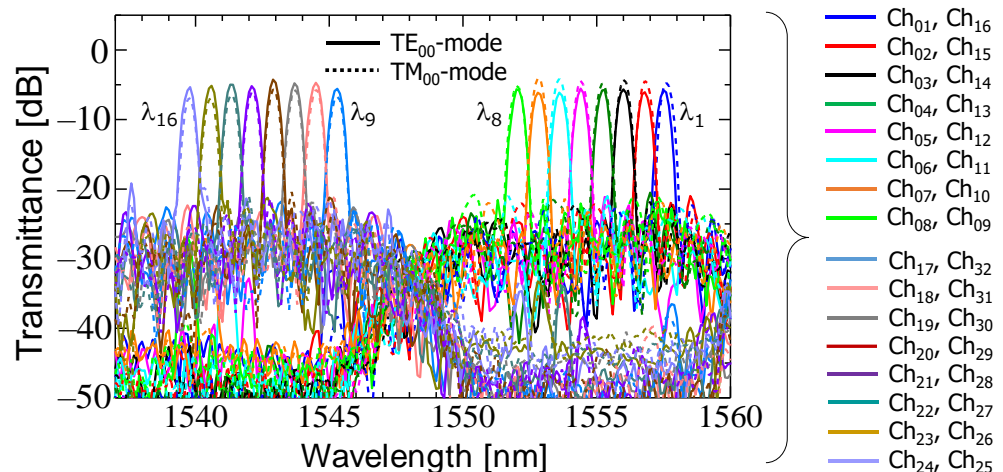


Figure 6. Measured 16λ optical DeMUX responses for TE_{00} -mode and TM_{00} -mode input signals.

For all output channels, the estimated peak transmittance ranged from -5 to -6 dB. It is noted that the transmittance shown in Figure 5 was estimated by subtracting the coupling loss of 2.5 dB/facet between lensed single-mode fibers and the two narrow-tapered spot-size conversion areas of the fabricated device. Consistent with findings from our previous studies [22,54], we attribute the entire excess loss to 0.5 dB from the PSR, 0.5 dB from the DI-based interleaver, and 4.5 dB from the AWG. Notably, optimization efforts, as detailed in our prior work [41], can potentially reduce the excess loss of the AWG to 1.2 dB. Experimental validation confirmed clear demultiplexing response for both linearly polarized lights. The measurement of 8λ spectra for both AWGs showed almost 0.8-nm-spaced (100-GHz). In Figure 6, the interleaver effectively suppressed one of periodic 8λ spectral groups spaced by the FSR of the AWGs, by more than 25 dB.

This facilitated the distinction of all 16 wavelength signals, regardless of the input signal’s polarizations. However, a deviation of +5 nm from the simulation results was observed in the center wavelength (1555 nm) of the filter spectral group for λ_1 – λ_8 (Ch₀₁–Ch₁₆) due to fabrication imperfections, necessitating adjustment through the optimization of fabrication processes or the control of design parameters. Notably, the filtering grids for each polarization were nearly the same of <0.1 nm owing to the shared lightwave paths facilitated by counter-propagation-type AWGs [42]. Furthermore, the two separate AWGs demonstrated nearly the same 8λ spectral responses including the AWG’s FSR, reflecting the precision achievable with 300 nm wafer-scale ArF-immersion lithography [54]. For all output channels, polarization-dependent loss (PDL) was evaluated to <0.5 dB.

We also verified device functionality by implementing 32 Gbps NRZ (non-return to zero) WDM signal transmissions through the fabricated chip. Figure 7 displays the calibrated eye patterns for the 32 Gbps NRZ signals (PRBS $2^{31}-1$) with TE₀₀- and TM₀₀-mode inputs at all output channels. An optical source was provided by a tunable single-mode diode laser, and the NRZ modulated signal was generated using a commercial optical modulator. We controlled the input signal’s polarization properly. Subsequently, we launched each signal into the device through a polarization maintaining fiber. The output signal was detected using an optical oscilloscope.

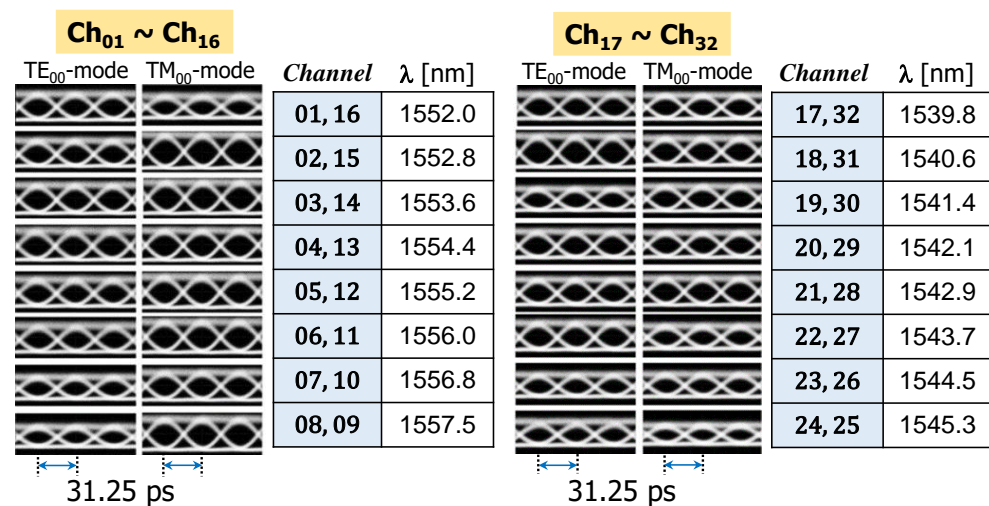


Figure 7. Measured eye patterns for 32 Gbps WDM signals (PRBS $2^{31}-1$) for the fabricated 16λ optical DeMUX for TE₀₀-mode and TM₀₀-mode input signals, together with operating channel specifications and output channel positions.

As depicted in Figure 7, we verified the functionality of the optical DeMUX by transmitting 32 Gbps NRZ modulated signals through it. We were able to confirm the clear opening of the eye diagrams at all output channels regardless of the input polarization states. It is important to note that the data rate was constrained solely by local experimental equipment. In the fabricated device, 3 dB filtering spectral widths for all outputs, as

depicted in Figure 6, were evaluated to be >0.42 nm, indicating the processing capability of the device up to >50 GHz of modulation bandwidth. In fact, we also observed clear eye openings for 50 Gbps NRZ modulated signals in similar transmission experiments.

As outlined in Ref. [49], the 16λ optical DeMUX is a fully passive device, with its properties dictated by the phase relation of spatial light interferences across several optical paths within numerous DIs and AWGs. Consequently, the filter’s spectral response, including center wavelength and spectral crosstalk, is greatly affected by the fabrication technology. Given the high phase accuracy provided by the adopted 300 mm SOI wafer-scale ArF-immersion lithography process along the interaction lengths within DIs and AWGs, the static and dynamic spectral characteristics depicted in Figures 6 and 7 remained consistent across the SOI wafer.

Meanwhile, the functionality of the 16λ optical DeMUX operation was not confined to the C-band spectral regime. Similar spectral characteristics were also experimentally verified in the O-band region. To adapt the device for O-band operation while maintaining single-mode conditions and considering chromatic dispersions between the DI-type interleaver and the AWG, adjustments were made only to the waveguide widths within each DI on the same SOI wafer used for the C-band option. Further details are available in Ref. [49].

Table 1 provides a comparative analysis of various DWDM-like multi-channel optical DeMUXs. In contrast to single-filtering type devices documented in [19,44], the depicted device in Figure 5 demonstrates reduced IL, increased channel count, and decreased spectral crosstalk. Furthermore, there was no report of polarization handling required in the receiver end for the combination-type devices [45,46], where an additional DI-based component interleaves AWG’s filtering spectra into even and odd wavelength parts. Only the proposed device scheme features polarization handling based on polarization diversity. When compared to silicon-nanowire-based devices, the proposed solution exhibits superior properties in terms of excess loss despite narrow channel spacing. Moreover, compared to a microring resonator-type device, the proposed scheme holds the possibility of additional channel count expansion. By adopting a 1×N (N: integer) type flatband DI-based interleaver [21,22] with a 1×M (M: integer) AWG, the total channel count could be scaled to N × M.

Table 1. Performance comparison for DWDM-like multi-channel optical DeMUXs.

	This Work [49]	Ref. [44]	Ref. [45]	Ref. [46]	Ref. [19]
Material system	Silicon	Silicon	Silica	Silicon	Si
Device scheme	DI + AWG	AWG	DI + AWG	DI + AWG	Microring
Principle	AWG group interleaving	Single filter	AWG odd/even interleaving		Single filter
PDL	<0.5 dB		NA (TE-mode only)		
Channel count	16	8	64	18	32
Chip size	4.76 mm ²	1 mm ²	49 mm ²	0.12 mm ²	2.2 mm ²
Channel spacing	100 GHz	100 GHz	25 GHz	200 GHz	100 GHz
Excessive loss	<6 dB	<5.5 dB	<6 dB	<10 dB	<5 dB
λ crosstalk for one channel	−34.6 to −19.5 dB	<−17 dB	<−30 dB	<−18 dB	<−15 dB

4. 800-GHz-Spaced 8λ LR-8 Optical DeMUX

Among the various data transmission specifications within short-reach interconnect datacenters, the 400GBASE-LR8 has emerged as a prominent standardization technology for 10 km reach employing SMFs, garnering active investigation [33,34,38,60,61]. In the context of LR-8 targeted WDM interconnects, each operational grid is discretely delineated in the O-band region [33,38]. A silica-based flatband AWG-type optical filter has been reported as an optical DeMUX for LR-8 optical interconnect applications [38]. In this setup, the discrete output channel relation was achieved by asymmetrically positioning the output waveguide arrays in the second half of the slab area. However, a number of challenges

persisted. The AWG typically has a large device size and inherently large IL caused by the optical spill over at the slab areas. Additionally, achieving flatband spectral response necessitated the use of multimode access waveguides in the slab region. Consequently, it is extremely difficult to employ the device architecture on the transmitter side. Moreover, a silica-based material platform is not appropriate for integrating with other silicon-based active components such as optical modulators and photodetectors.

Thus far, efforts have been made to address the aforementioned limitations by introducing a silicon-nanowire-based optical DeMUX employing cascade-connected DIs [33]. Here, although the discrete LR-8 spectral relation was attained by controlling a certain optical path difference at the third-stage DI, the suppression rate of unwanted spectral components at around $\lambda = 1291$ nm was as high as -4 dB. In addition, the spectral response exhibited a Gaussian-function shape, which may not be suitable for practical applications.

To address lingering technical challenges, we introduced and theoretically validated a non-Gaussian box-like spectral-optical DeMUX scheme intended for LR-8 400GbE data-center applications [34].

Figure 8 illustrates the schematic diagram of the LR-8 targeted optical DeMUX, along with the specified operating grids and the position of the required phase shift within each DI [$PS_1 = 1.0\pi$ (rad.), $PS_2 = 0.5\pi$ (rad.), $PS_3 = 0.25\pi$ (rad.)]. The device needs four-stage multiple DIs. While eight wavelengths can be spatially filtered out without the fourth-stage DI [21], adherence to conventional design guidelines [21,22] did not align the operating wavelength grid with the LR-8 grid due to the cyclic spectral nature of multi-stage DIs. In contrast, in a prior study [33], the deliberate adjustment of one of the optical path differences at the third-stage DI to half compared to others aimed at breaking the aforementioned cyclic spectral nature, thus allowing alignment with each LR-8 grid. However, despite clear spectral differences around $\lambda = 1291$ nm, the spectral noises remained unacceptably high at approximately -4 dB. This prompted the adoption of the fourth-stage DI in the optical DeMUX configuration.

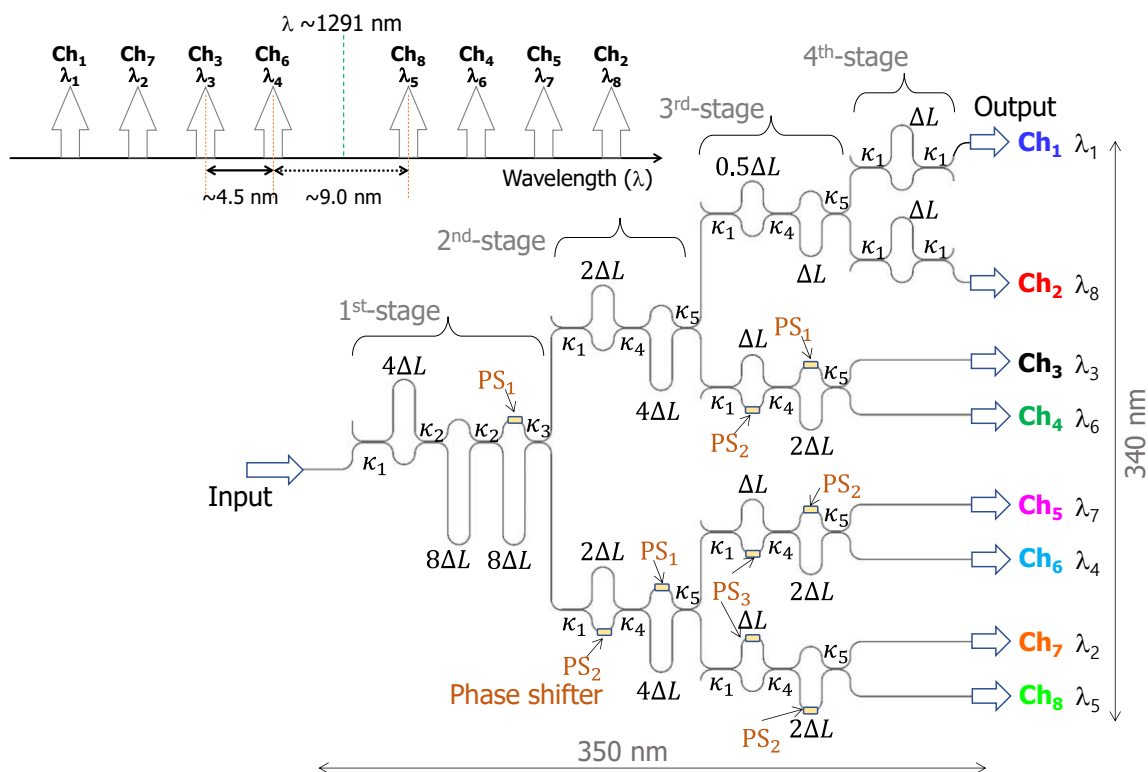


Figure 8. Schematic of silicon-nanowire-type DI-based optical DeMUX for LR-8 400GbE transmission, together with LR-8 WDM channel positions.

In this case, the fourth-stage DI serves to cut out the unwanted spectral range at around $\lambda = 1291$ nm, thus reducing spectral crosstalk to less than -20 dB. To achieve this filtering operation, the optical path differences for the third and fourth DIs of Ch-1 and Ch-2 were appropriately optimized to completely out of phase at around $\lambda = 1291$ nm. Meanwhile, remaining device parameters in the proposed device were adjusted to achieve a flatband spectral response, as described in prior works [21,22]. The first delayed Mach–Zehnder interferometer with integer multiple values ($=4\Delta L, 2\Delta L, \Delta L$) at all DI stages defines all central filtering peaks. In addition, cascade-connected multiple interferometers at all DI stages create a box-like spectral shape, accomplished by properly adjusting coupling ratios at each DI stage ($\kappa_1 = 0.5; \kappa_2 = 0.2; \kappa_3 = 0.04; \kappa_4 = 0.33; \text{ and } \kappa_5 = 0.08$) and each optical path difference. As depicted in Figure 1, the silicon-nanowire-based proposed scheme implies a total chip size of $350 \mu\text{m}$ in length and $340 \mu\text{m}$ in width.

The LR-8 optical DeMUX scheme’s spectral response was modeled using the scattering matrix method and coupled mode theory [21–24]. The wavelength-sensitive coupling ratios of silicon-nanowire directional couplers (DCs) were formulated, and their spectral validity was corroborated by the previous data [24]. As the waveguide structure, we designed 350-nm -wide and 220-nm -thick silicon-nanowire channel waveguides operating in the O-band region. The separation gap of each DC was uniformly designed as $0.2 \mu\text{m}$, adhering to standard conditions in the currently available CMOS-based foundry process. Following these design guidelines, various DC splitting ratios were numerically simulated using the 3D-BPM method (BeamPROP™; Synopsys, CA, USA). Subsequently, their outcomes were integrated into the main loop of the scattering matrix for the multiple DI-type optical DeMUX.

Figure 9 illustrates the computed spectral properties of LR-8 channels: (a) a conventional box-like spectral optical DeMUX based on multiple DIs [21], (b) a Gaussian-shaped DI-based DEMUX achieved through local path difference control at the third-stage DI [33], (c) the design combination described in Refs. [21,33], and (d) the proposed DI-based optical DeMUX incorporating extra band elimination filters [34]. It is noted that the path differences for each DeMUX were commonly set to maintain an inter-channel gap of 800 GHz.

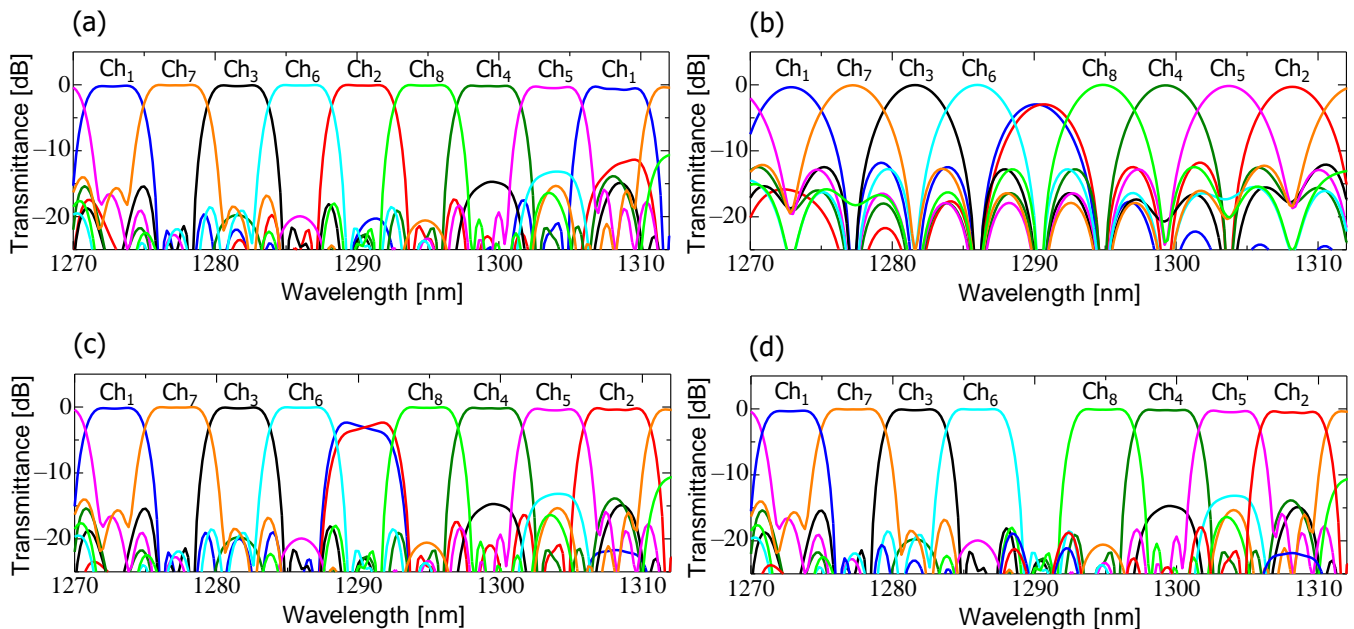


Figure 9. Analyzed LR-8 spectral response for (a) conventional box-like spectral DI-DEMUX, (b) Gaussian-shaped DI-DEMUX utilizing the local path difference control at the third-stage DI, (c) the design combination for Refs. [21–33], and (d) the proposed DI-DEMUX.

In Figure 9a, achieving flatband involves cascade-connecting excessive interferometers at each DI stages. The operating window is inclined to show an equidistant spacing of 800 GHz, resulting in a difficulty in discriminating LR-8 optical signals. In Figure 9b, the proper control of the path difference at the third-stage DI inhibits the unwanted band at approximately $\lambda = 1291$ nm [33]. However, the extinction ratio (ER) is not small enough to maintain a sufficiently low WDM system penalty. Figure 9c demonstrates that combining the design strategies from Figure 9a,b provides spectral distinction with a box-like spectral response. Nevertheless, it is noted that an inadequate ER of <4 dB still remains. Figure 9d shows that the proposed LR-8 DeMUX dramatically relaxes the drawback on ER to >20 dB without compromising the quality of the flatband spectral response. Further enhancements such as reducing the wavelength dependence of DC coupling efficiency or incorporating multimode interference (MMI) couplers would make the proposed LR-8 DeMUX more practical in applications.

Table 2 provides a comparative analysis of various LR-8 targeted optical DeMUXs. In contrast to previously reported devices documented in [33,38], the proposed device illustrated in Figure 8 offers numerous advantages in terms of small footprint, low IL, spectral crosstalk at around $\lambda = 1291$ nm, spectral flatness, and other factors. Compared to silicon-nanowire-based devices, the proposed scheme exhibits superior spectral qualities, albeit requiring experimental verification. Needless to say, integration with the PSR alongside the LR-8 optical DeMUXs enables the detection of arbitrarily polarized LR-8 optical signals based on polarization diversity, as experimentally evidenced in Figures 6 and 7.

Table 2. Performance comparison for LR-8 targeted optical DeMUXs.

	This Work [34]	Ref. [38]	Ref. [33]
Material	Si-nanowire	Silica	Si-nanowire
Chip size	0.12 mm ²	70 mm ² #	0.3 mm ²
Insertion loss	1.5 dB #	1.5 dB	3.5 dB
Crosstalk at $\lambda = 1.29$ μ m	<−20 dB	<−20 dB	<−4 dB
Spectral shape	Flat-topped	Flat-topped	Gaussian
Experimental demonstration	Not yet	Performed	Performed

Expected values.

5. 20-nm-Spaced 4 λ CWDM Optical DeMUX

CWDM provides many advantages over DWDM due to its less strict prerequisites for the accurate control of diode laser oscillation frequency and broader available operating range in the wavelength domain. Additionally, CWDM devices must properly work within a wavelength range exceeding 60 nm, as the operating point is spaced by 20 nm [5–7,11]. Furthermore, the optical DeMUX at the receiver’s end must possess the capability to handle arbitrary polarization input signals [28,30,35,36,40,42,47,49]. To date, various methods have been investigated to manage randomly polarized CWDM signals for use in the optical receiver, which can be categorized into three groups: the zero-birefringence scheme [28], the polarization compensation scheme [30,40], or the polarization diversity schemes [35,36,47,49], applied to silicon nitride (SiN) [28,40,47] and silicon (Si) [30,35,36,49] materials.

The zero-birefringence scheme finds extensive application within SiN material systems [28], employing square-like core shapes to eliminate wavelength sensitivities of the split/coupling response and achieve nearly identical equivalent index in optical waveguides. Despite experimental validations of the zero-birefringence in the SiN waveguides, there still remains nonnegligible spectral discrepancy between the TE₀₀ and TM₀₀ modes. SiN-based AWG based on polarization-compensation has also been deployed for use in CWDM systems [40], enabling operation regardless of the input polarizations through lateral asymmetric-core-shaped polarization rotators within each arrayed waveguide of the AWG. Nonetheless, additional study is required to overcome drawbacks such as large

device size, relatively small fabrication margin for polarization rotators, and the complexity of monolithic integration to silicon-nanowire-based components.

Additionally, a silicon-nanowire-type CWDM DeMUX was reported [30], due mainly to its compactness and feasibility of monolithic integration. The polarization issue associated with silicon-nanowire waveguides has been addressed through the implementation of the polarization compensation scheme. In this scenario, lateral asymmetric waveguide-based polarization rotators were located in the middle of all single-stage DIs. These components rotate the polarization by 90 degrees whenever the signal traverses each DI, facilitating the depolarization of the spectral response for all input polarizations. Achieving this involves utilizing a 340 nm thick silicon core layer to depolarize the optical split and coupling behavior of the bending-type DC. However, a thick core (beyond the standard value of 220 nm) may lead to technical difficulty in making the nanowire's propagation loss lower. Moreover, the polarization rotators necessitate extreme precision in the lithography process such as electron beam lithography, rendering them unattractive for good productivity.

Overall, as mentioned earlier, in terms of polarization-handling CWDM DeMUXs, SiN-based devices exhibited issues such as spectral non-uniformity [28], substantial footprint exceeding millimeter-scale lengths, and intricate fabrication processes [40], along with challenges in integrating monolithically with silicon-nanowire-based devices [62]. On the other hand, concerns regarding higher excess loss for propagation and increased manufacture precision due to a thicker core were raised for silicon-nanowire-based devices [30]. Consequently, there have been few publications on silicon-nanowire-based polarization-handling CWDM DeMUXs.

Figure 10 depicts the fabricated polarization-diversified CWDM optical DeMUXs: (a) lacking TM_{00} -mode rejection filters and (b) incorporating TM_{00} -mode rejection filters. These devices typically incorporate a PSR to introduce polarization diversity, along with two DI-type optical DeMUXs of identical design for CWDM optical signal filtering. The design principles and operational concept of the PSR mirror those shown in Figure 1. In instances where a mode split area relies on a rectangle-shaped silicon-nanowire ADC, a relatively narrower waveguide is linearly tapered, as depicted in Figure 3b. Consequently, incident WDM signals with varied linear polarization states, such as combinations of TE_{00} -mode and TM_{00} -mode, are divided into the TE_{00} -mode signals and directed to spatially separated output channels of the ADC [35].

The DI-based optical DeMUX is composed of three optical delaylines, each with adjusted path differences to achieve constructive interference at each CWDM grid, along with two identical 50:50 MMI couplers. It is crucial to emphasize that the optical DeMUX must span a wavelength range exceeding 60 nm. Therefore, MMI couplers were chosen over DCs, which exhibit sinusoidal coupling behaviors, to serve as optical couplers in each DI. The width of the silicon-nanowire waveguide in each DI, excluding the MMI region, was designed to be $W_{CH} = 350$ nm.

The fabrication of the CWDM optical DeMUXs involved utilizing the ArF-dry lithography process on a 200 mm SOI wafer featuring a 220-nm-thick silicon core layer and a 2- μ m-thick BOX layer. The mode split region in the PSR employed the L-ADC, considering the possible phase accuracy from the foundry process and the limitations of the feasible photomask design. To assess the filter spectral response, a tunable laser served as the optical source. The transmittance of the manufactured devices was calibrated using an optical vector analyzer (OVA) (OVA 5013; LUNA Innovations, VA, USA). Analyzing the Jones matrix of the output transmitted signals enabled the examination of the transmittance response from arbitrarily linear-polarized inputs to each type of output via SMFs [63,64].

In the measurement of the single-mode fiber-based optical transmittance of the fabricated devices, the temperature of the device was controlled to 25 degrees Celsius. It has been well known that, compared with the case for silicon dioxide, the refractive index change for single-crystalline silicon is much more sensitive to external temperature variation by a factor of 10 [65–68]. Since silicon has a relatively large thermo-optic coefficient of 1.8×10^{-4} [1/K] [65], the filter spectral peak for various kinds of optical DeMUXs tends to

shift to the longer wavelength side by up to 0.07 [nm/K] as the temperature increases. Since the 4λ 20-nm-spaced DeMUXs have a relatively wider operating wavelength range, the temperature variation of 50 degrees Celsius (plus or minus 25 degrees Celsius) can be tolerable without any significant spectral penalties in terms of IL and spectral crosstalk. Meanwhile, the temperature-sensitive nature of silicon stimulated extensive work on energy-efficient thermal tuning by forming micro heaters on the silicon-nanowire waveguides [69–71].

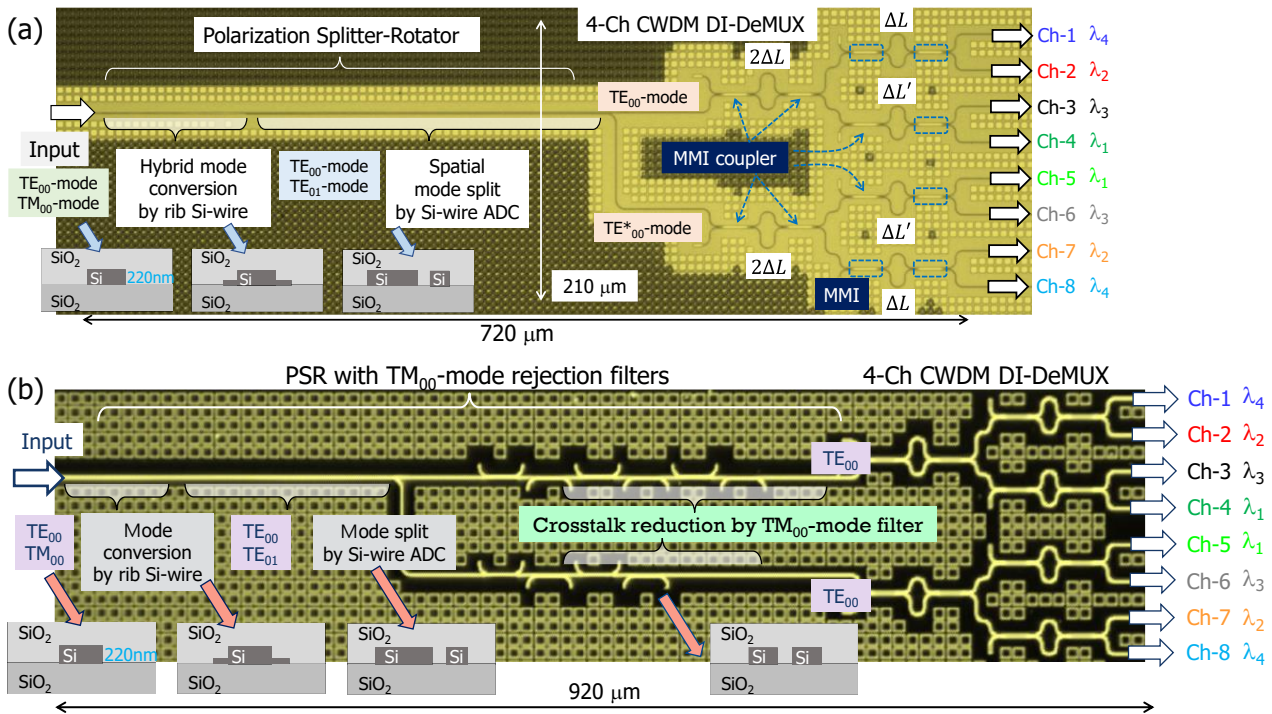


Figure 10. Fabricated polarization-diversified CWDM DeMUXs: (a) without TM_{00} -mode elimination areas and (b) integrated with TM_{00} -mode elimination areas.

Initially, we assessed the transmission spectra of the fabricated device depicted in Figure 10a. The spectra for all outputs spanning Ch-1 to Ch-8 are illustrated in Figure 11. The following spectra shown in Figure 11a–d were provided by the OVA: (a) main signals (TE_{00} -mode input to TE_{00} -mode output for Ch-1–Ch-4, TM_{00} -mode input to TE_{00} -mode output for Ch-5–Ch-8), (b) cross-coupled spectral noises (TM_{00} -mode input to TE_{00} -mode output for Ch-1–Ch-4, TE_{00} -mode input to TE_{00} -mode output for Ch-5–Ch-8), (c) TE_{00} -to- TM_{00} -mode polarization spectral noises (TE_{00} -mode input to TM_{00} -mode output for all outputs), and (d) TM_{00} -to- TM_{00} -mode polarization spectral noises (TM_{00} -mode input to TM_{00} -mode output for all outputs).

As seen in Figure 11a, we were able to experimentally validate CWDM demultiplexing spectra whose output responses are nearly depolarized. All outputs displayed *sinc*-function-shaped nearly ideal response, spaced by 20 nm, indicating the spatial separation of the TE_{00} -mode input from the upper output of the PSR without undergoing any hybrid mode change, and directed into the upper-sided DeMUX. Conversely, TM_{00} -mode inputs were confirmed at outputs from Ch-5 to Ch-8. In spite of the pronounced structural birefringence of the silicon-nanowire waveguide, we clearly observed closely resembling spectra, which specifies that only the TM_{00} -mode components experienced hybrid mode change to TE_{01} -mode, with its propagation mode then being split as the TE_{00} -mode in the L-ADC. As a result, random polarized signals were effectively discriminated within the 60-nm-wide spectral window, showcasing an excessive loss of <1.0 dB and a PDL of <1.0 dB. That is, excessive loss indicates the extra loss incurred compared to the propagation loss of bending-shaped nanowires with the same length, accounting for losses stemming from hybrid mode change, spatial mode split, and MMI interactions. Spectral noises coming

from adjacent nanowires were evaluated at -20 dB for the peak transmittance of each four outputs.

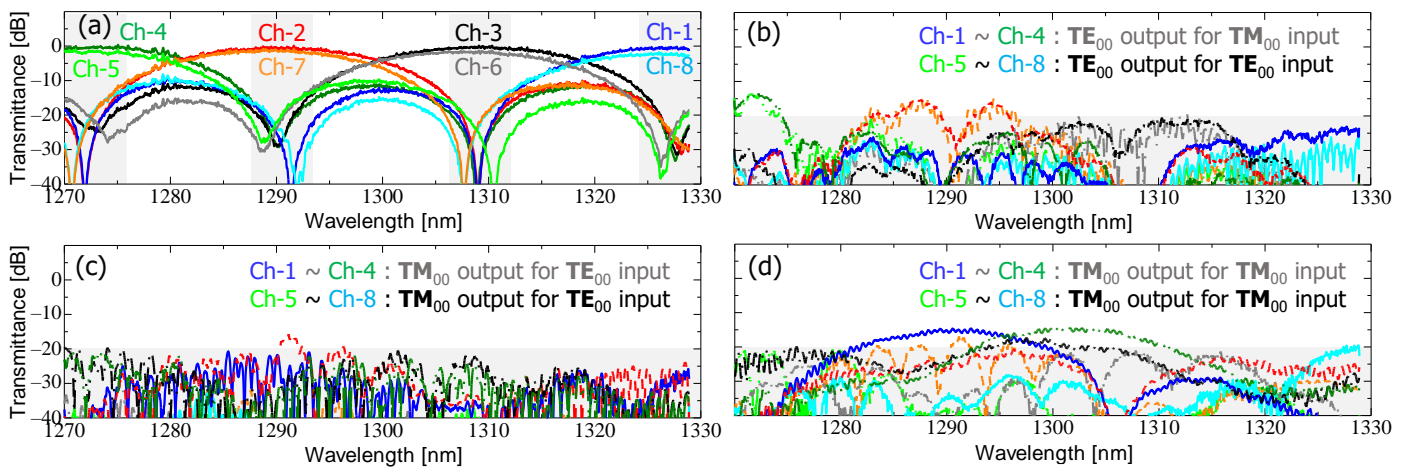


Figure 11. Measured spectral characteristics of the fabricated device shown in Figure 10a: (a) main signals (TE_{00} -mode input to TE_{00} -mode output for Ch-1–Ch-4, TM_{00} -mode input to TE_{00} -mode output for Ch-5–Ch-8), (b) cross-coupled spectral noises, (c) TE_{00} -to- TM_{00} -mode polarization spectral noises, and (d) TM_{00} -to- TM_{00} -mode polarization spectral noises.

The measured responses in Figure 11b–d illustrate different forms of spectral noises. In a sense, these response levels should be thoroughly minimized because they are not necessary at all. Somewhat elevated residual polarization spectral noises observed in the PSR result from inadequate mode change in the shallow-edged waveguide region and an insufficient mode split efficiency in the L-ADC, especially concerning TM_{00} -to- TM_{00} -mode polarization spectral noises.

To make clear those concerns, TM_{00} -mode elimination cutters, utilizing a cascade-connection of symmetric DCs, were sequentially attached to the PSR. We tested the polarization-diversified optical DeMUX integrated with TM_{00} -mode elimination cutters (depicted in Figure 10b). In Figure 12a, it is evident that the primary signals were filtered out regardless of their polarizations. Moreover, the transmission of the cross-coupled spectral noises was blocked by <-20 dB across the entire O-band region, which is similar to the outcome seen in Figure 11b. Additionally, measured spectra involving the integration of external filter arrays with the PSR (shown in Figure 12c,d) exhibited a notable suppression of >20 dB in TM_{00} -mode-related polarization spectral noises compared to the data depicted in Figure 12c,d.

It is noted that the spectral properties for the main signals and cross-coupled noises presented in Figure 12a,b exhibit some degree of inferiority compared to those shown in Figure 11a,b, particularly concerning excessive loss, spectral uniformity, and spectral noise level. This discrepancy is not attributable to the presence of TM_{00} -mode elimination cutters but rather stems from fabrication imperfections. These problems are most likely due to the shallow-etched nanowire structure, influenced by the double patterning process impacting hybrid mode change, and the channel waveguide shape, affected by dry etching processes impacting pattern width accuracy compared to the design and fabrication, as well as the magnitude of statistical random phase deviations at each DMZI, contingent upon line edge roughness. We believe that these fabrication imperfections are a temporary drawback. Once again, such double patterning structures can be managed by the commercially available silicon photonics foundry process [55]. Considering more advanced lithography technologies as explained in Ref. [54], we believe that the double patterning structures would be no obstacle for densely integrated high-performance circuits.

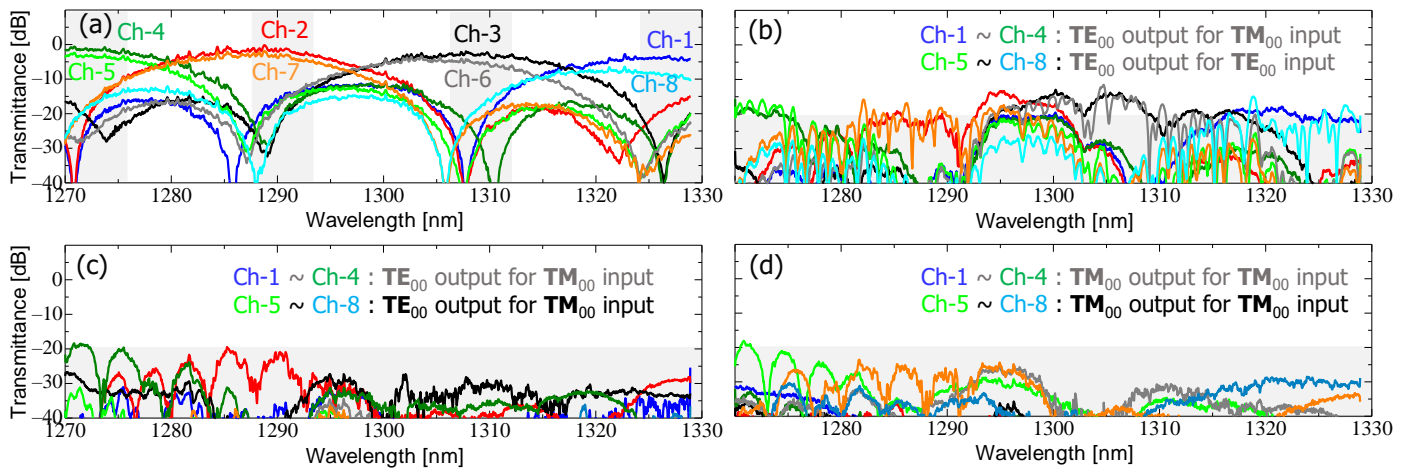


Figure 12. Measured spectral characteristics of the fabricated device shown in Figure 10b: (a) main signals (TE_{00} -mode input to TE_{00} -mode output for Ch-1–Ch-4, TM_{00} -mode input to TE_{00} -mode output for Ch-5–Ch-8), (b) cross-coupled spectral noises, (c) TE_{00} -to- TM_{00} -mode polarization spectral noises, and (d) TM_{00} -to- TM_{00} -mode polarization spectral noises.

The devices depicted in Figure 12a,b exhibited distinct spectra because they were manufactured on different SOI substrates at different points in time. As illustrated in Figure 12a, the excess loss at each filtering wavelength slightly increased as the wavelength shifted towards the longer wavelength side. These phenomena could be attributed to fabrication errors, leading to the MMI width being narrower than intended in the photomask design. Consequently, a narrower MMI width caused the optimal split and coupling conditions to shift to the shorter wavelength side, occurring at approximately $\lambda = 1.26 \mu\text{m}$. On the other hand, the degraded spectral uniformity and relatively high PDL were associated with statistically increased random phase errors at each DI. We anticipate that the meticulous management of the fabrication procedure will resolve these shortcomings.

Lastly, Table 3 provides a comparative analysis of various types of polarization-handling-based CWDM optical DeMUXs. Compared to previously reported studies [28,30,40], the proposed optical DeMUX demonstrated spectral advantages regarding device footprint, IL, and polarization crosstalk. As mentioned earlier, it is worth noting that the reason for the inferior IL and PDL observed in the proposed device scheme integrated with TM_{00} -mode rejection filters was primarily due to fabrication imperfections rather than the integration of the TM_{00} -mode rejection filters. As indicated in Table 3, a SiN-based optical DeMUX based on Echelle grating was also reported [72]. Based on different propagation constants and diffraction conditions for TE_{00} -mode and TM_{00} -mode input signals in the Echelle grating region, the diffracted CWDM output signals were filtered out to spatially separated output channels. Among SiN-based optical DeMUXs, this one features a small footprint by utilizing the folded back interaction in the Echelle grating.

Table 3. Performance comparison for polarization-handling-based CWDM optical demultiplexers.

	This Work ¹	Ref. [30]	Ref. [28]	Ref. [40]	Ref. [72]
Material	Si-nanowire	Si-nanowire	SiN	SiN	SiN
Principle	Cascade-connected Multiple DIs			AWG	Echelle
Chip size	0.2 mm ²	0.3 mm ²	2.25 mm ²	1.1 mm ²	0.41 mm ²
IL	<2 dB	<2 dB	<3.5 dB	<2 dB	<2.5 dB
PDL	<3 dB	<0.1 dB	<1.5 dB	<1 dB	<1.8 dB
λ crosstalk ²	<−15 dB	<−18 dB	<−15 dB	<−25 dB	<−25 dB
Pol. Crosstalk ³	<−25 dB	NA ⁴	NA ⁴	NA ⁴	<−20 dB
Flat spectra	No	Yes	Yes	No	No
Grid match ⁵	Good	Good	Bad	Bad	Bad

¹ Proposed device integrated with TM_{00} -mode elimination cutters [36]. ² Wavelength crosstalk from adjacent nanowires. ³ TM_{00} -mode-induced spectral noises from the PSR. ⁴ No experimental data were shown for polarization crosstalk. ⁵ Degree of grid matching from four CWDM channels.

For satisfying the requirements of practical interconnect applications for integrated components, optical DeMUXs with a box-like response are highly desirable. This allows for simplified operation control for laser sources. In the case of the DI-based device scheme, achieving such a need involves connecting additional DIs with diverse coupling efficiencies and path differences to modify the scattering matrices of the DI-based interferometers [21,22,28,30].

6. Summary

We present an overview of our recent research activities focused on three types of silicon-nanowire-based optical DeMUXs tailored for versatile high-density optical interconnect applications. Firstly, we delve into the discussion of polarization diversified 100-GHz-spaced 16λ optical DeMUXs, comprising 2λ DI-based interleavers and 8λ AWGs, within the spectral regimes of $1.55\ \mu\text{m}$ and $1.31\ \mu\text{m}$. Based on theoretical analyses, the proposed devices were fabricated by using an ArF-immersion-lithography-based 300 mm SOI waferscale platform. Experimental results demonstrated both static and dynamic spectral properties, together with further extendable channel scalability. Secondly, we explored an 800-GHz-spaced 8λ optical DeMUX tailored for LR-8 400Gbps Ethernet applications. This device, based on multiple cascade-connected DIs, incorporates additional band rejection filters to achieve non-continuous discrete filtering responses with box-like spectral responses and low spectral noises of $<-15\ \text{dB}$ across the full LR-8 operating window. Lastly, we discussed polarization-diversified optical DeMUXs aimed at CWDM applications. These were subjected to numerical analysis and experimental demonstration, showcasing an extremely small IL (1.0 dB) and a PDL (1.0 dB), effectively mitigating spectral noises from adjacent neighboring channels by $<-20\ \text{dB}$. Additionally, TM_{00} -mode elimination filters were devised prior to launching into each DeMUX to minimize residual TM_{00} -mode polarization crosstalk. As a result, the unwanted TM_{00} -mode-oriented polarization crosstalk originating from the polarization-handling device was managed to $<-20\ \text{dB}$ across the entire CWDM operating window.

Funding: The work on the 20-nm-spaced 4λ CWDM optical DeMUX was supported by a grant from the Electronics and Telecommunications Research Institute (ETRI), funded by the ICT R&D program of MSIT/IITP (2019-0-00002, Development of Optical Cloud Networking Core Technology). The work on the 800-GHz-spaced 8λ LR-8 optical DeMUX was supported by a research grant from the University of Suwon in 2022. The work on the 100-GHz-spaced 16λ DWDM optical DeMUX was based on results obtained from a project commissioned by the New Energy and Industrial Technology Development Organization (NEDO).

Data Availability Statement: Data underlying the results presented in this paper are not publicly available at the time of publication, but may be obtained from the author upon reasonable request.

Conflicts of Interest: The author declares no conflicts of interest.

References

1. Ram, C.F. Optical network technologies for datacenter networks. In Proceedings of the Optical Communication Conference, San Diego, CA, USA, 21–25 March 2010.
2. Essiambre, R.-J.; Tkach, R.W. Capacity trends and limit of optical communication networks. *Proc. IEEE* **2012**, *100*, 1035–1055. [[CrossRef](#)]
3. Zhao, X.; Vusirikala, V.; Koley, B.; Kamalov, V.; Hofmeister, T. The prospect of inter-data-center optical networks. *IEEE Commun. Magz.* **2013**, *51*, 32–38. [[CrossRef](#)]
4. Cheng, Q.; Bahadori, M.; Glick, M.; Rumley, S.; Bergman, K. Recent advances in optical technologies for data centers: A review. *Optica* **2018**, *5*, 1354–1370. [[CrossRef](#)]
5. Nebeling, M. CWDM transceivers. In *Coarse Wavelength Division Multiplexing Technologies and Applications*, 1st ed.; Thiele, H.-J., Nebeling, M., Eds.; CRC Press: Boca Raton, FL, USA, 2007; pp. 57–90.
6. Liu, A.; Liao, L.; Chetrit, Y.; Basak, J.; Nguyen, H.; Rubin, D.; Paniccia, M. Wavelength division multiplexing circuit on silicon-on-insulator platform. *IEEE J. Sel. Top. Quantum Electron.* **2010**, *16*, 23–32.
7. Hamdi, M.M.; Audah, L.; Rashid, S.A.; Al-Mashhadani, M.A. Coarse WDM in metropolitan networks: Challenges, standards, applications, and future role. *J. Phys.* **2020**, *1530*, 012062.

8. Vlasov, Y.A. Silicon CMOS-integrated nano-photonics for computer and data communications beyond 100G. *IEEE Commun. Mag.* **2012**, *50*, S67–S72. [[CrossRef](#)]
9. Doerr, C.R. Silicon photonic integration in telecommunications. *Front. Phys.* **2015**, *3*, 37. [[CrossRef](#)]
10. Absil, P.P.; Verheyen, P.; De Heyn, P.; Pantouvaki, M.; Lepage, G.; De Coster, J.; Van Campenhout, J. Silicon photonics integrated circuits: A manufacturing platform for high density, low power optical I/O's. *Opt. Express* **2015**, *23*, 9369–9378. [[CrossRef](#)] [[PubMed](#)]
11. Rosenberg, J.C.; Horst, F.; Khater, M.; Anderson, F.G.; Leidy, R.; Barwicz, T.; Gill, D.; Kiewra, E.; Martin, Y.; Orcutt, J.S.; et al. Monolithic silicon photonic WDM transceivers. In Proceedings of the European Conference on Optical Communications, Gothenburg, Sweden, 17–21 September 2017; pp. 1–3. [[CrossRef](#)]
12. Zhang, J.; Groote, A.D.; Abbasi, A.; Loi, R.; O'Callaghan, J.; Corbett, B.; José Trindade, A.; Bower, C.A.; Roelkens, G. Silicon photonics fiber-to-the-home transceiver array based on transfer-printing-based integration of III–V photodetectors. *Opt. Express* **2017**, *25*, 14290–14299. [[CrossRef](#)]
13. Timurdogan, E.; Su, Z.; Shiue, R.; Byrd, M.J.; Poulton, C.V.; Jabon, K.; DeRose, C.; Moss, B.R.; Hosseini, E.S.; Duzevik, I.; et al. 400G silicon photonics integrated circuit transceiver chipsets for CPO, OBO, and pluggable modules. In Proceedings of the Optical Fiber Communication Conference, San Diego, CA, USA, 8–12 March 2020. T3H.2.
14. Aoki, T.; Sekiguchi, S.; Simoyama, T.; Tanaka, S.; Nishizawa, M.; Hatori, N.; Sobu, Y.; Sugama, A.; Akiyama, T.; Hayakawa, A.; et al. Low-crosstalk simultaneous 16-channel \times 25Gb/s operation of high-density silicon photonics optical transceiver. *IEEE Lightw. Technol.* **2018**, *36*, 1262–1267. [[CrossRef](#)]
15. Akiyama, T.; Oda, S.; Jeong, S.-H.; Nakasha, Y.; Hayakawa, A.; Tanaka, Y.; Hoshida, T. An Extremely low-crosstalk WDM demultiplexer with an automatic error-correction capability enabling temperature insensitivity and high-yield integration on low-end Si PICs. In Proceedings of the 45th European Conference on Optical Communication (ECOC 2019), Dublin, Ireland, 22–26 September 2019.
16. Wang, H.; Dai, J.; Jia, H.; Shao, S.; Fu, X.; Zhang, L.; Yang, L. Polarization-independent tunable optical filter with variable bandwidth based on silicon-on-insulator waveguides. *Nanophotonics* **2018**, *7*, 1469–1477. [[CrossRef](#)]
17. Kumar, R.R.; Tsang, H.K. High-extinction CROW filters for scalable quantum photonics. *Opt. Lett.* **2021**, *46*, 134–137. [[CrossRef](#)] [[PubMed](#)]
18. Morichetti, F.; Milanizadeh, M.; Petrini, M.; Zanetto, F.; Ferrari, G.; de Aguiar, O.; Guglielmi, E.; Sampietro, M.; Melloni, A. Polarization-transparent silicon photonic add-drop multiplexer with wideband hitless tuneability. *Nat. Commun.* **2021**, *12*, 4324. [[CrossRef](#)] [[PubMed](#)]
19. Deng, Q.; El-Saeed, A.H.; Elshazly, A.; Lepage, G.; Marchese, C.; Kobbi, H.; Magdziak, R.; Coster, J.D.; Singh, N.; Filipic, M.E.; et al. 32×100 GHz WDM filter based on ultra-compact silicon rings with a high thermal tuning efficiency of $5.85 \text{ mW}/\pi$. *arXiv* **2024**, arXiv:2311.12036. [[CrossRef](#)]
20. Kim, D.W.; Barkai, A.; Jones, R.; Elek, N.; Nguyen, H.; Liu, A. Silicon-insulator eight-channel optical multiplexer based on a cascade of asymmetric Mach–Zehnder interferometers. *Opt. Lett.* **2008**, *33*, 530–532. [[CrossRef](#)] [[PubMed](#)]
21. Horst, F.; Green, W.M.J.; Assefa, S.; Shank, S.M.; Vlasov, Y.A.; Offrein, B.J. Cascaded Mach-Zehnder wavelength filters in silicon photonics for low loss and flat pass-band WDM (de-)multiplexing. *Opt. Express* **2013**, *21*, 11652–11658. [[CrossRef](#)] [[PubMed](#)]
22. Jeong, S.H.; Shimura, D.; Simoyama, T.; Horikawa, T.; Tanaka, Y.; Morito, K. Si-nanowire-based multistage delayed Mach-Zehnder interferometer optical MUX/DeMUX fabricated by an ArF-immersion lithography process on a 300 mm SOI wafer. *Opt. Lett.* **2014**, *39*, 3702–3705. [[CrossRef](#)] [[PubMed](#)]
23. Jeong, S.H.; Morito, K. 1×4 channel Si-nanowire microring-assisted multiple delayline-based optical MUX/DeMUX. *IEEE J. Light. Technol.* **2015**, *33*, 3736–3743. [[CrossRef](#)]
24. Jeong, S.H.; Tanaka, Y. Silicon-wire optical demultiplexers based on multistage delayed Mach–Zehnder interferometers for higher production yield. *Appl. Opt.* **2018**, *57*, 6474–6480. [[CrossRef](#)] [[PubMed](#)]
25. Chang, L.; Gong, Y.; Liu, L.; Li, Z.; Yu, Y. Low-loss broadband silicon-on-insulator demultiplexers in the O-band. *IEEE Photonics Technol. Lett.* **2017**, *29*, 1237–1240. [[CrossRef](#)]
26. Gao, G.; Chen, D.; Tao, S.; Zhang, Y.; Zhu, S.; Xiao, X.; Xia, J. Silicon nitride O-band (de)multiplexers with low thermal sensitivity. *Opt. Express* **2017**, *25*, 12260–12267. [[CrossRef](#)]
27. Tao, S.; Huang, Q.; Zhu, L.; Liu, J.; Zhang, Y.; Huang, Y.; Wang, Y.; Xia, J. Athermal 4-channel (de-)multiplexer in silicon nitride fabricated at low temperature. *Opt. Express* **2018**, *6*, 686–691. [[CrossRef](#)]
28. Mikkelsen, J.C.; Bois, A.; Lordello, T.; Mahgerefteh, D.; Menezo, S.; Poon, J.K.S. Polarization-insensitive silicon nitride Mach-Zehnder lattice wavelength demultiplexers for CWDM in the O-band. *Opt. Express* **2018**, *26*, 30076–30084. [[CrossRef](#)] [[PubMed](#)]
29. Xu, H.; Shi, Y. Flat-top CWDM (De)Multiplexer based on MZI with bent directional couplers. *IEEE Photon. Technol. Lett.* **2018**, *30*, 169–172. [[CrossRef](#)]
30. Xu, H.; Liu, L.; Shi, Y. Polarization-insensitive four-channel coarse wavelength-division (de)multiplexer based on Mach–Zehnder interferometers with bent directional couplers and polarization rotators. *Opt. Lett.* **2018**, *43*, 1483–1486. [[CrossRef](#)] [[PubMed](#)]
31. Xu, H.; Dai, D.; Shi, Y. Low-crosstalk and fabrication-tolerant four-channel CWDM filter based on dispersion-engineered Mach-Zehnder interferometers. *Opt. Express* **2021**, *29*, 20617–20631. [[CrossRef](#)] [[PubMed](#)]
32. Yen, T.H.; Hung, Y.J. Fabrication tolerant CWDM (de)multiplexer based on cascaded Mach-Zehnder interferometers on silicon-on-insulator. *J. Light. Technol.* **2021**, *39*, 146–153. [[CrossRef](#)]

33. Zhao, Z.; Li, Z.; Nui, J.; Zhang, G.; Chen, H.; Fu, X.; Yang, L. Eight-channel LAN WDM (De)Multiplexer based on cascaded Mach-Zehnder interferometer on SOI for 400GbE. *Photonics* **2022**, *9*, 252. [[CrossRef](#)]
34. Jeong, S.H. Flat-band 8-channel optical MUX/DeMUX for long reach 400GbE applications. In Proceedings of the 22nd International Conference on Numerical Simulation of Optoelectronic Devices, Torino, Italy, 12–16 September 2022. IS08.
35. Jeong, S.H.; Park, H.; Lee, J.K. Polarization insensitive CWDM optical demultiplexer based on polarization splitter-rotator and delayed interferometric optical filter. *Curr. Opt. Photon.* **2023**, *7*, 166–175.
36. Jeong, S.H.; Park, H.; Lee, J.K. Silicon-nanowire-type polarization-diversified CWDM demultiplexer for low polarization crosstalk. *Nanomaterials* **2023**, *13*, 2382. [[CrossRef](#)]
37. Pathak, S.; Vanslebrouck, M.; Dumon, P.; Van Thourhout, D.; Bogaerts, W. Optimized silicon AWG with flattened spectral response using an MMI aperture. *J. Light. Technol.* **2013**, *31*, 87–93. [[CrossRef](#)]
38. Doi, Y.; Nakanishi, Y.; Yoshimatsu, T.; Ohno, T.; Sanjo, H. Compact 8-wavelength receiver optical sub-assembly with a low-loss AWG demultiplexer for 400-gigabit datacom. In Proceedings of the 2015 European Conference on Optical Communication (ECOC), Valencia, Spain, 27 September–1 October 2015. [[CrossRef](#)]
39. Gehl, M.; Trotter, D.; Starbuck, A.; Pomerene, A.; Lentine, A.L.; Derose, C. Active phase correction of high resolution of silicon photonic arrayed waveguide gratings. *Opt. Express* **2017**, *25*, 6320–6334. [[CrossRef](#)] [[PubMed](#)]
40. Guerber, S.; Alonso-Ramos, C.A.; Le Roux, X.; Vulliet, N.; Cassan, E.; Marris-Morini, D.; Boeuf, F.; Vivien, L. Polarization independent and temperature tolerant AWG based on a silicon nitride platform. *Opt. Lett.* **2020**, *45*, 6559–6562. [[CrossRef](#)] [[PubMed](#)]
41. Okayama, H.; Onawa, Y.; Shimura, D.; Takahashi, H.; Yaegashi, H.; Sasaki, H. Low loss 100GHz spacing arrayed-waveguide grating using minimal terrace at slab-array interface. *Electron Lett.* **2016**, *52*, 1545–1546. [[CrossRef](#)]
42. Onawa, Y.; Okayama, H.; Shimura, D.; Takahashi, H.; Yaegashi, H.; Sasaki, H. Polarisation insensitive wavelength de-multiplexer using arrayed waveguide grating and polarisation rotator/splitter. *Electron Lett.* **2019**, *55*, 475–476. [[CrossRef](#)]
43. Smit, M.K.; Dam, V.C. PHASAR-based WDM-devices: Principles, design and applications. *IEEE J. Sel. Top. Quantum Electron.* **1996**, *2*, 236–250. [[CrossRef](#)]
44. Wang, J.; Sheng, Z.; Li, L.; Pang, A.; Wu, A.; Li, W.; Wang, X.; Zou, S.; Qi, M.; Gan, F. Low-loss and low-crosstalk 8×8 silicon nanowire AWG routers fabricated with CMOS technology. *Opt. Express* **2014**, *22*, 9395–9403. [[CrossRef](#)] [[PubMed](#)]
45. Abe, M.; Hibino, Y.; Tanaka, T.; Itoh, M.; Himeno, A.; Ohmori, Y. Mach-Zehnder interferometer and arrayed waveguide-grating integrated multi/demultiplexer with photosensitive wavelength tuning. *Electron. Lett.* **2001**, *37*, 376–377. [[CrossRef](#)]
46. Chen, S.; Fu, X.; Wang, J.; Shi, Y.; He, S.; Dai, D. Compact dense wavelength-division (de)multiplexer utilizing a bidirectional arrayed-waveguide grating integrated with a Mach-Zehnder interferometer. *IEEE J. Light. Technol.* **2015**, *33*, 2279–2286. [[CrossRef](#)]
47. Chen, L.; Doerr, C.; Chen, Y. Polarization diversified DWDM receiver on silicon free of polarization dependent wavelength shift. In Proceedings of the Optical Fiber Communication Conference, Los Angeles, CA, USA, 24–28 March 2012; OW3G.
48. Fang, Q.; Jia, L.; Song, J.; Li, C.; Luo, X.; Yu, M.; Lo, G. A high-crosstalk silicon photonic arrayed waveguide grating. *Proc. Int. J. Electron. Commun. Eng.* **2016**, *10*, 372–373.
49. Jeong, S.H.; Onawa, Y.; Shimura, D.; Okayama, H.; Aoki, T.; Yaegashi, H.; Horikawa, T.; Nakamura, T. Polarization diversified 16 λ demultiplexer based on silicon wire delayed interferometers and arrayed waveguide grating. *J. Light. Technol.* **2020**, *38*, 2680–2687. [[CrossRef](#)]
50. Dai, D.; Liu, L.; Gao, S.; Xu, D.-X.; He, X. Polarization management for silicon photonic integrated circuits. *Laser Photon. Rev.* **2012**, *7*, 303–328. [[CrossRef](#)]
51. Sacher, W.D.; Barwicz, T.; Taylor, B.J.F.; Poon, J.K.S. Polarization rotator-splitters in standard active silicon photonics platforms. *Opt. Express* **2014**, *22*, 3777–3786. [[CrossRef](#)]
52. Xu, H.; Shi, Y. Ultra-broadband silicon polarization splitter-rotator based on the multi-mode waveguide. *Opt. Express* **2017**, *25*, 18485–18491. [[CrossRef](#)] [[PubMed](#)]
53. Selvaraja, S.; Murdoch, G.; Milenin, A.; Delvaux, C.; Ong, P.; Pathak, S.; Vermeulen, D.; Sterckx, G.; Winroth, S.; Verheyen, P.; et al. Advanced 300-mm wafer-scale patterning for silicon photonics devices with record low loss and phase errors. In Proceedings of the Opto-Electronics and Communications Conference, Shanghai, China, 28 June–2 July 2015; p. 15.
54. Horikawa, T.; Shimura, D.; Okayama, H.; Jeong, S.H.; Takahashi, H.; Ushida, J.; Sobu, Y.; Tokushima, M.; Kinoshita, K.; Mogami, T. A 300-mm silicon photonics platform for large-scale device integration. *IEEE J. Light. Technol.* **2018**, *24*, 8200415. [[CrossRef](#)]
55. Siew, S.Y.; Li, B.; Gao, F.; Zheng, H.Y.; Zhang, W.; Guo, P.; Xie, S.W.; Song, A.; Dong, B.; Luo, L.W.; et al. Review of silicon photonics technology and platform development. *J. Light. Technol.* **2021**, *39*, 4374–4389. [[CrossRef](#)]
56. Xu, H.; Dai, D.; Shi, Y. Ultra-broadband and ultra-compact on-chip silicon polarization beam splitter by using hetero-anisotropic metamaterials. *Laser Photonics Rev.* **2019**, *13*, 1800349. [[CrossRef](#)]
57. Meng, Y.; Chen, Y.; Lu, L.; Ding, Y.; Cusano, A.; Fan, J.A.; Hu, Q.; Wang, K.; Xie, Z.; Liu, Z.; et al. Optical meta-waveguides for integrated photonics and beyond. *Light Sci. Appl.* **2021**, *10*, 235. [[CrossRef](#)] [[PubMed](#)]
58. Huang, C.; Huang, C. Ultra-compact and high-performance polarization beam splitter assisted by slotted waveguide subwavelength gratings. *Sci. Rep.* **2020**, *10*, 12841. [[CrossRef](#)]

59. Meng, Y.; Liu, Z.; Xie, Z.; Wang, R.; Qi, T.; Hu, F.; Kim, H.; Xiao, Q.; Fu, X.; Wu, Q.; et al. Versatile on-chip light coupling and (de)multiplexing from arbitrary polarizations to controlled waveguide modes using an integrated dielectric metasurface. *Photonics Res.* **2020**, *8*, 564–576. [[CrossRef](#)]
60. Zhou, Y.R.; Smith, K.; Gilson, M.; Brooks, P.; Cole, C.; Yu, C. Field and laboratory trials of 400GBASE-LR8 over fibre distances up to 35 km. *IET Electron. Lett.* **2018**, *54*, 1288–1290. [[CrossRef](#)]
61. Yue, Y.; Wang, Q.; Yao, J.; O’Neil, J.; Pudvay, D.; Anderson, J. 400 GbE technology demonstration using CFP8 pluggable modules. *Appl. Sci.* **2018**, *8*, 2055. [[CrossRef](#)]
62. Maegami, Y.; Okano, M.; Cong, G.; Ohno, M.; Yamada, K. Completely CMOS compatible SiN-waveguide-based fiber coupling structure for Si wire waveguides. *Opt. Express* **2016**, *24*, 16856–16865. [[CrossRef](#)] [[PubMed](#)]
63. Gifford, D.K.; Soller, B.J.; Wolfe, M.S.; Froggatt, M.E. Optical vector network analyzer for single-scan measurements of loss, group delay, and polarization mode dispersion. *Appl. Opt.* **2005**, *44*, 7282–7286. [[CrossRef](#)] [[PubMed](#)]
64. Kim, J.H.; Adams, D.B.; Madsen, C.K. Device-under-test Jones matrix extraction algorithm with device TE/TM reference frame. *IEEE Photon. Technol. Lett.* **2012**, *24*, 88–90. [[CrossRef](#)]
65. Coenen, D.; Oprins, H.; Ban, Y.; Ferraro, F.; Pantouvaki, M.; Campenhout, J.V.; Wolf, I.D. Thermal modelling of silicon photonic ring modulator with substrate undercut. *J. Light. Technol.* **2022**, *40*, 4357–4363. [[CrossRef](#)]
66. Gylfason, K.B.; Romero, A.M.; Sohlström, H. Reducing the temperature sensitivity of SOI waveguide-based biosensors. In Proceedings of the SPIE Optical Engineering, Brussels, Belgium, 10 May 2012. [[CrossRef](#)]
67. Guan, X.; Frandsen, L.H. All-silicon interferometer with multimode waveguides for temperature-insensitive filters and compact biosensors. *Opt. Express* **2019**, *27*, 753–760. [[CrossRef](#)] [[PubMed](#)]
68. Hiraki, T.; Fukuda, H.; Yamada, K.; Yamamoto, T. Small sensitivity to temperature variations of Si-photonic Mach–Zehnder interferometer using Si and SiN waveguides. *Front. Mater.* **2015**, *2*, 00026. [[CrossRef](#)]
69. Lee, J.M.; Kim, D.K.; Kim, G.H.; Kwon, O.K.; Kim, K.J.; Kim, G. Controlling temperature dependence of silicon waveguide using slot structure. *Opt. Express* **2008**, *16*, 1645–1652. [[CrossRef](#)]
70. Dong, P.; Qian, W.; Liang, H.; Shafiiha, R.; Feng, D.; Li, G.; Cunningham, G.E.; Krishnamoorthy, A.V.; Asghari, M. Thermally tunable silicon racetrack resonators with ultralow tuning power. *Opt. Express* **2010**, *18*, 20298–20304. [[CrossRef](#)]
71. Padmaraju, K.; Bergman, B. Resolving the thermal challenges for silicon microring resonator devices. *Nanophotonics* **2014**, *3*, 269–281. [[CrossRef](#)]
72. Li, C.; Xiong, B.; Chu, T. Polarization-independent wavelength demultiplexer based on a single etched diffraction grating device. *Commun Eng.* **2023**, *2*, 4. [[CrossRef](#)]

Disclaimer/Publisher’s Note: The statements, opinions and data contained in all publications are solely those of the individual author(s) and contributor(s) and not of MDPI and/or the editor(s). MDPI and/or the editor(s) disclaim responsibility for any injury to people or property resulting from any ideas, methods, instructions or products referred to in the content.